

Predicting the chemical homogeneity in laser powder bed fusion (LPBF) of mixed powders after remelting

Huikai Li, Erin G. Brodie, Christopher Hutchinson*

Department of Materials Science and Engineering, Monash University, Victoria 3800, Australia



ARTICLE INFO

Keywords:

Additive manufacturing
Laser powder bed fusion
Duplex stainless steel
Compositional distribution
Remelting

ABSTRACT

An advantage of laser powder bed fusion (LPBF) of metals is that one can create topologically complex components with comparative ease. Most LPBF studies use commercial pre-alloyed powders and less attention has been given to new alloy design for LPBF. Physical mixing of powders with different chemistries can be an effective way to access new alloy compositions for LPBF without the need for custom pre-alloyed powders. In this work, a previously published model to describe the chemical distribution of LPBF material from mixed powders is extended to the process of remelting and is quantitatively compared with experiment. A mix of Ni and stainless steel powders is used to assess the effect of remelting on the chemical homogeneity and the model is shown to agree well with experiment once evaporation of selected species and changes in melt pool size during remelting are incorporated. Strategies to improve the chemical homogeneity of prints from mixed powders are discussed. Remelting is one approach but the chemical homogeneity improves only marginally after three remelts. The critical role of the melt pool size compared to the minority powder particle spacing is emphasised. Finally, an example of using spatially controlled chemical homogeneity to create architected materials using LPBF is shown.

1. Introduction

The overwhelming majority of published research using LPBF use commercially available pre-alloyed powders. 316 L stainless steel, nickel alloy 625, aluminium alloy Al10MgSi and titanium alloy Ti64 have been the most popular. As a consequence, the research emphasis has largely been on process optimisation, types of printing defects and the resulting properties that can be obtained, in both the as-built state and after subsequent heat treatments.

There has been comparatively less emphasis on new alloy design specifically for the LPBF process. This is a particularly interesting direction because none of the most popular readily available pre-alloyed powders were originally designed for LPBF. The comparative lack of activity on new alloy design is understandable. Few research groups have the ability to make their own small batch, pre-alloyed powder and hence experimental efforts to test ideas about new alloys for LPBF is difficult. During the last 10 years, there has been a large increase in the number of research groups physically mixing powders to study new alloy compositions for LPBF [1]. This is also sometimes called in-situ alloying, or blended powders. The idea is to physically mix readily

available powders (elemental, or pre-alloyed, or a combination) so that the overall composition matches the desired new composition. Often this powder mixing is performed in bottles on a tube roller, sometimes ball milling is used, and in other cases special processes have been developed to attach a 2nd powder to the primary powder by a process referred to as satelliting [1,2]. Powder mixing has now been used in almost all alloy classes as a way to access new alloy compositions. The most activity has been on Ti alloys [2–32] but examples can also be found in steels [33–37], high entropy alloys (HEA) [38–41], nickel alloys [42–48], magnesium alloys [49–52], aluminium alloys [53–62], and Mn-based and W-based alloys [63–65].

The powder mixing approach to access new alloy compositions for LPBF is effective if the chemical composition of the printed part is a good approximation of the new composition being targeted. This depends strongly on the chemical mixing of the powders in the melt pool during printing and the resulting chemical homogeneity in the build. Some authors have reported examples of very good chemical mixing and a relatively homogeneous chemical distribution in the printed part, but there are many cases where substantial chemical heterogeneity exists after printing. The easiest cases of heterogeneity to understand are the

* Corresponding author.

E-mail address: crh@monash.edu (C. Hutchinson).

examples where a powder of comparatively high melting point element (e.g. refractory element) is added to a much lower melting point powder. Examples are Mo, Nb or Ta additions to Ti alloys [3–8,14,25,27–32]. In these cases, it is often observed that the higher melting point powder does not fully dissolve in the melt pool and particles of that powder can be found in the final build. However, even in cases where the mixed powders do fully melt, there are many cases where the resulting chemical composition in the as-built product contains significant chemical heterogeneity as a result of different melt pool chemistries due to different mixed powder compositions being sampled at different positions of the laser, e.g. [66]. The general observations are that chemical homogeneity can be improved by decreasing the laser scan speed (e.g. [10,38,48]), increasing the laser energy (e.g. [14,38,58]), or by remelting [5,6,43]. These efforts are a reflection of the community asking how the chemical homogeneity can be controlled, either through process control, or through the preparation of the powder mixtures.

Li et al. [66] recently presented a model to describe the probability distribution for the chemical homogeneity in the as-built state using LPBF of mixed powders. The approach assumed only a random powder distribution in the starting state and full chemical mixing in the melt pool (i.e. it assumes the powders dissolve in the melt pool). Whilst these authors were interested in taking advantage of deliberate chemical heterogeneity in the as built state, and other authors have also recently highlighted the interest in deliberately heterogeneous materials [23,34], the model presented was able to predict the chemical heterogeneity as a function of both laser scan speed and scan line overlap. The key physical quantity being varied by changes in the processing was the melt pool size, and the importance of this quantity for chemical mixing and the resulting homogeneity has also been highlighted by other authors [38, 58]. Better chemical mixing is obtained with bigger melt pool sizes because the larger melt pool size includes more powder and as the volume of powder being melted increases, it approaches a better approximation to the overall powder chemistry. However, there are limits to the melt pool sizes that can be accessed in practice, either due to power constraints of the laser, or constraints around printing defect control. Remelting steps have been shown to improve the homogeneity of the local chemistries found in builds made from mixed powders [5,6, 43], but there is currently no guidance on what remelting strategies should be used. The objective of this contribution is to fill that gap in knowledge.

In this work, we extend the model presented by Li et al. [66] to describe the chemical distribution after LPBF of mixed powders, to the process of remelting. We use a mix of 22Cr duplex stainless steel and pure Ni powders to experimentally test the effect of remelting on the resulting chemical distribution. This work provides insight to the remelting (and printing) strategies that are worth pursuing for those interested in using mixed powders as a means of sampling new alloy compositions in LPBF.

2. Experimental procedure

2.1. Materials

This work uses a mixed powder. The mixture is comprised of pure Ni

powder (6 wt%) and the balance is 22Cr duplex stainless steel powder (SAF2205–22Cr). The Ni powder was procured from TLS Technik GmbH & Co., Germany. The stainless steel powder was purchased from Sandvik Osprey Ltd, UK. The manufacturer reported particle size distributions and powder chemistries are listed in Table 1 (rows 1 and 2). The composition of the 22Cr-6Ni powder mixture, calculated from the compositions of the individual powders is shown as the third row of Table 1. The chemical composition of a printed sample from the 22Cr-6Ni mixture has been measured by ICP-AES and this composition is shown in the fourth row of Table 1. It shows excellent agreement with the composition calculated from the manufacturer reported powder compositions. The powder mixture was prepared by rotating PE bottles containing the mixed powder for 48 h on a tube roller.

2.2. Printing

An M-Lab Cusing R LPBF machine (Concept Laser) with a Nd:YAG laser, maximum power of 100 W and 50 µm spot size, was used for the printing. A 316 L plate was used as the substrate for the builds. Optimised parameters (i.e. porosity < 0.2%) for printing included a 90 W laser power, 150 mm/s laser scan speed, hatch spacing of 120 µm and 15 µm layer thickness. A remelting strategy, which consisted of multiple laser passes before a new layer of powder is applied (Fig. 1) was investigated as a tool to improve the chemical homogeneity of mixed powder prints. Two geometric variations of remelting were examined. The first strategy consisted of a 90° rotation between remelting laser scans. A second remelting scan pattern was explored with a 67° rotation between layers, ensuring no direct overlap in laser scan tracks would occur during subsequent remelting scans.

Zero remelt refers to initial powder melting for material consolidation (i.e. the usual additive manufacturing consolidation process) and the maximum number of remelts attempted was six. All prints were performed with a nitrogen atmosphere and oxygen content below 0.2%.

10 mm side length cubes, obtained using the 90° rotation remelting strategy, and cylinders with a size of φ 10 mm × 10 mm, obtained using the 67° rotation remelting strategy, were used for microstructural and chemical characterisation.

2.3. Microstructural characterisation

Samples were sectioned along the build direction (x-z plane) from the cube centre line for microstructural analysis. Surfaces for optical observation of the melt pool morphology were ground to P4000 grit, polished with 3 µm diamond suspension and then etched with 10% aqueous oxalic acid. A Leica DM 750 M optical microscope was used for imaging. In all cases, the porosities of the builds, even after remelting, were extremely low and below 0.2%.

A JEOL scanning electron microscope (JSM-7001 F) was used for microstructure and chemistry characterisation. Electron backscattered diffraction (EBSD) was performed on a plane in the middle of the sample parallel to the build direction for the characterisation of phase, grain size, and texture. The chemical distribution was measured on the same plane containing the build direction using energy-dispersive X-ray spectroscopy (EDS). A working distance of 10 mm and an accelerative

Table 1

Compositions (wt%) and sizes (µm) of SAF2205 stainless steel and pure Ni powders, as reported by the supplier. The composition of the physical mixture of SAF2205 + 6%Ni (wt%) is calculated based on the compositions of the individual powders. The Printed 2205 + 6.0Ni (0 remelt): ICP-AES sample corresponds to an experimental measurement using ICP-AES demonstrating agreement with the composition expected.

Alloy	Cr	Ni	Mo	Mn	Si	N	C	Fe	D10	D50	D90
SAF2205	22.5	5.5	3.2	1.3	0.9	0.21	0.02	Bal.	17.8	31.7	55.2
Pure Ni	-	99.8	-	-	-	-	< 0.008	< 0.01	25.0	38.7	54.9
SAF2205 + 6.0 Ni	21.2	11.2	3.0	1.2	0.8	0.20	0.02	Bal.	-	-	-
Printed 2205 + 6.0Ni (0 remelt): ICP-AES	21.1 ± 0.25	11.5 ± 0.20	2.93 ± 0.12	1.05 ± 0.07	0.65 ± 0.06	0.14 ± 0.02	0.01	Bal	-	-	-

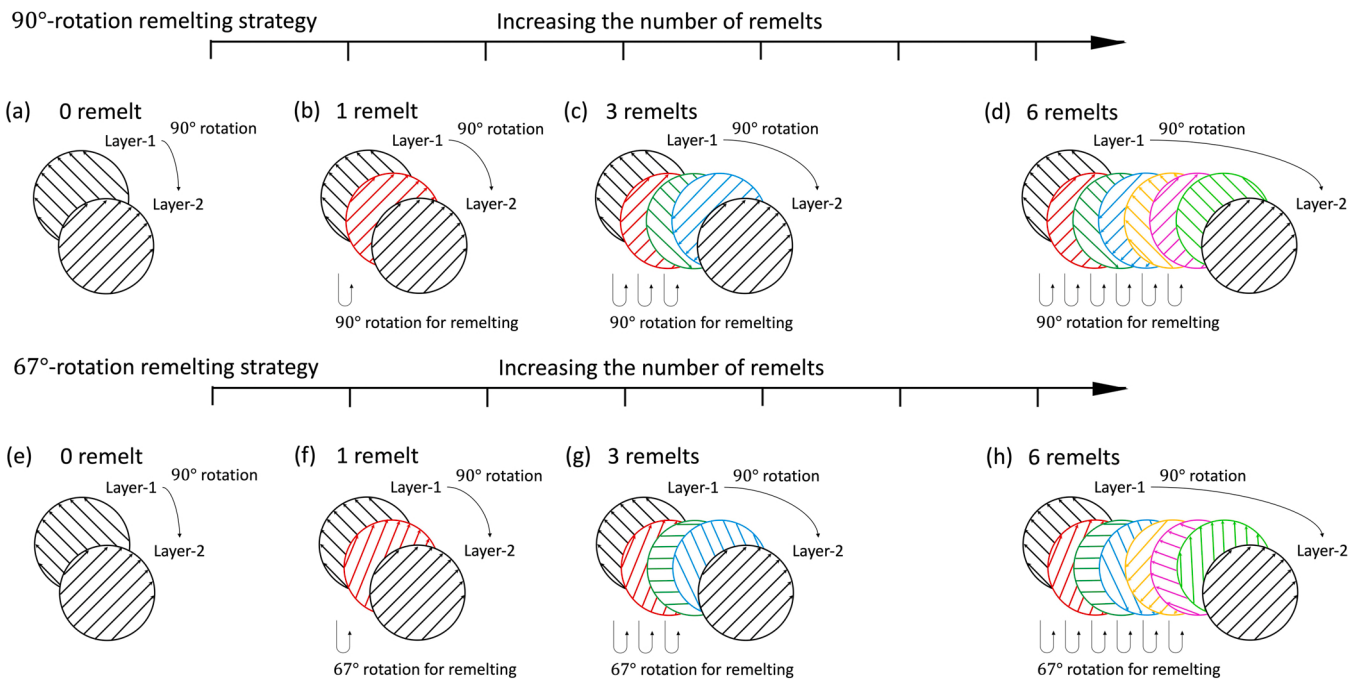


Fig. 1. Schematic illustration of remelting strategies: (a) 90°-rotation 0 remelt, (b) 90°-rotation 1 remelt, (c) 90°-rotation 3 remelts, (d) 90°-rotation 6 remelts, (e) 67°-rotation 0 remelt, (f) 67°-rotation 1 remelt, (g) 67°-rotation 3 remelts, (h) 67°-rotation 6 remelts.

voltage of 15 kV was used for the EDS measurements. Three vertical EDS line scans (ie. aligned in the build direction) each covering 1.0 mm length were performed. One line was centred exactly at the middle height of the sample and the other two lines were centred at $\frac{1}{4}$ and $\frac{3}{4}$ height. The EDS spectra of 200 points in each line were collected, with a point separation of 5.0 μm . The EDS detector is Oxford Instruments X-Max 80 Silicon Drift type. Pixel dwell time is 15 s for each data point to control the statistical error in the measured Ni content at < 0.3 wt%.

The surfaces were ground to P4000 grit, then polished with 3 μm and 1 μm diamond suspension, followed by OPS.

In addition, since the builds were performed in a nitrogen atmosphere, the nitrogen content was measured by LECO combustion as a function of remelting steps to monitor for any nitrogen pick-up during the process (none was observed). This is important because nitrogen is a strong austenite (FCC) stabiliser and can affect the phase formation observed in our microstructures.

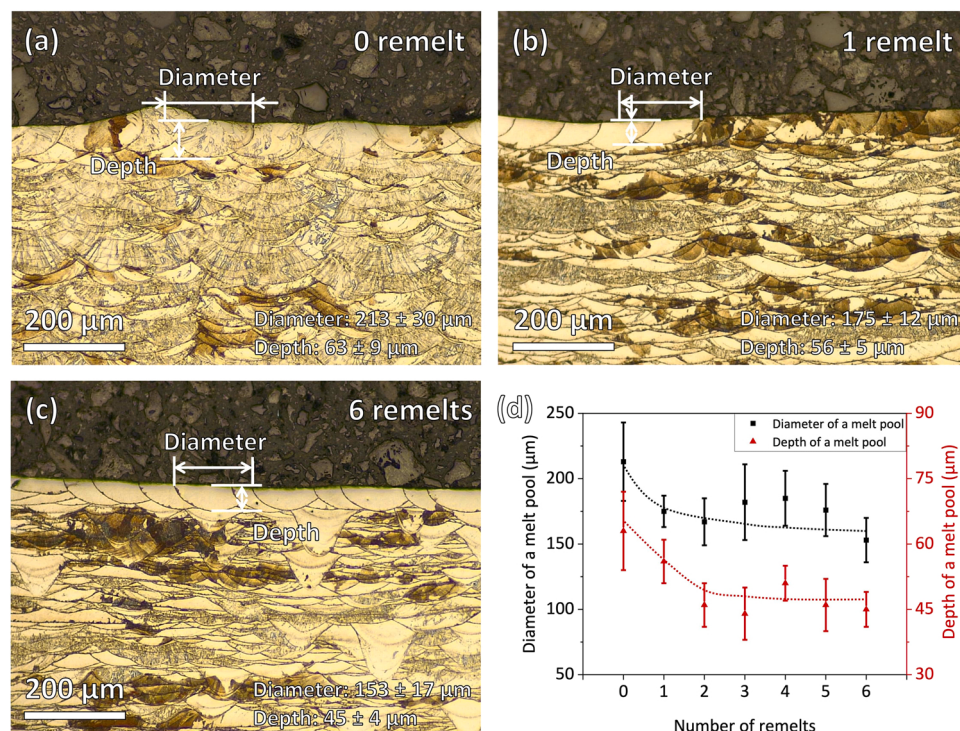


Fig. 2. Optical micrographs of 22Cr-6Ni showing the melt pool size for (a) 0 remelt, (b) 1 remelt, and (c) 6 remelts of the cubic samples built using the 90° remelt rotation strategy. (d) Dimensions of melt pool size with increasing remelts.

3. Results

3.1. Melt pool size

The macroscopic geometry of the melt pool for 0, 1 and 6 remelts is shown in Fig. 2a-c for the cubic samples built using the 90° remelt strategy. Melt pool size, characterised by diameter and depth, was measured from the top layer of the sample, where the melt pools are most clearly defined. Each measurement of diameter and depth is the average of between 25 and 30 measurements taken from five different images of the magnification shown in Fig. 2a-c. The error bars represent ± 1 standard deviation. It is assumed the melt pool is symmetric and the depth of a melt pool is the distance between the lowest point of the melt pool to the top. The melt pool size in the 0 remelt process is larger in both diameter and depth than the melt pools created by remelting steps. The average depth of the melt pool decreases from 0 to 6 remelts, as shown in Fig. 2d. A drop from $\sim 63 \mu\text{m}$ to $\sim 45 \mu\text{m}$ is observed between the 0 remelt and 2 remelt conditions. Thereafter, the depth stabilises.

The diameter of the melt pool displays a similar trend. At 0 remelt, the average diameter of a melt pool is $\sim 213 \mu\text{m}$, and this decreases to a size of $\sim 153 \mu\text{m}$ after 6 remelts.

The optical micrographs shown in Fig. 2 may give the impression of a poor quality etch – with some dark regions appearing locally. There are two effects that give rise to this impression – the first is that the microstructures shown in Fig. 2 contain both ferritic (BCC) and austenitic (FCC) regions (as will be shown in the following section) and these etch differently. The second important point is that even within one phase, the chemical composition varies from position to position and this also affects the response to the etch. Whilst the heterogeneity of the etch in optical microscopy shown in Fig. 2 may give the impression of poor etching technique, it is actually a reflection of the spatial heterogeneity of the structure and chemistry of the build from the mixed powders. We have chosen to use optical microscopy for Fig. 2 so that the reader is able to see the low magnification view of the heterogeneous structure arising from printing of mixed powders.

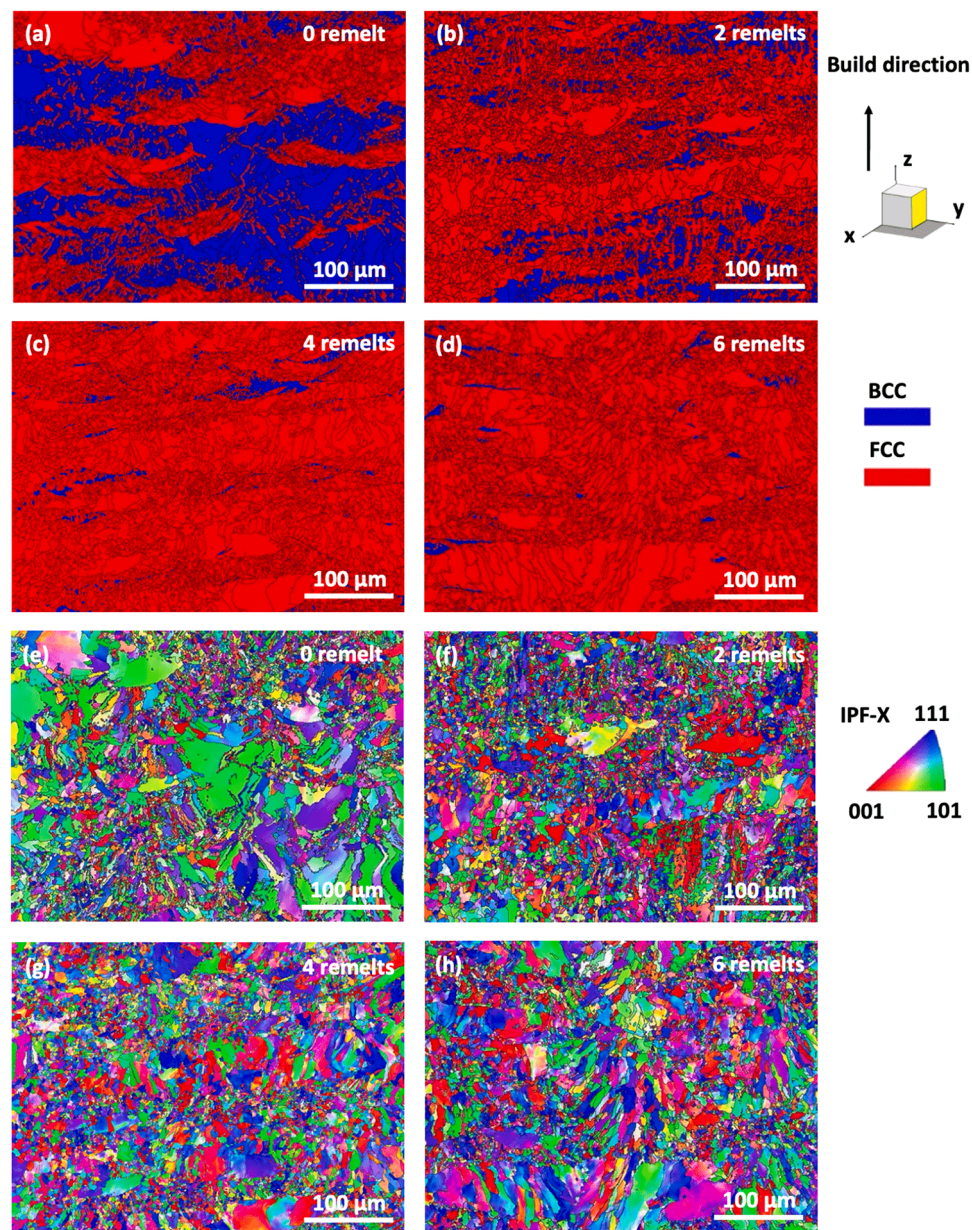


Fig. 3. Phase identification maps (a-d) and inverse pole figure maps (e-h) for the 22Cr-6Ni structures from 0 remelt, 2 remelts, 4 remelts and 6 remelts using the 90°-rotation remelting strategy.

3.2. Phase distribution

Despite 22Cr being a duplex stainless steel alloy composition, it is well known that when produced by LPBF, the material is fully BCC (ferrite) in the as-built state [67–69]. The Ni is an austenite stabiliser in the melt pools where the Ni content is high, producing regions of FCC (austenite). Electron back scattered diffraction (EBSD) was used to reveal the phase evolution as a result of the increased number of remelts. The FCC volume fraction increased with the increasing number of remelts. Fig. 3a shows an approximately 50/50 FCC/BCC structure in the 0 remelt condition. With the increase of the number of remelts, the FCC volume fraction increases and the fine grained FCC regions become connected (Fig. 3b-c and f-g). With 6 remelts (Fig. 3d and h), a fully FCC structure is present with a mixture of both fine equiaxed and coarse elongated FCC grains.

To demonstrate that the regions of FCC are Ni-rich and those that are BCC are Ni-poor, an EDS linescan has been made across a FCC+BCC region shown in Fig. 4. As shown in Fig. 4b, the blue regions of the EBSD map, corresponding to BCC, are those containing a locally low concentration of Ni.

3.3. Chemical compositional distribution

To quantitatively analyse the effect of remelting on the chemical distribution, EDS measurements of the Ni content in the remelted microstructures are shown in Fig. 5. As shown previously [66], a critical Ni content of 10.0–10.3 wt% is required for austenite to form (instead of ferrite) during cooling using mixed powders of 22Cr-6Ni in LPBF. 600 point EDS measurements, from 3 different 1.0 mm line scans per sample, are binned (0.5% Ni) and plotted as cumulative distributions in Fig. 5. Fig. 5a-h shows the effect of remelting on the probability distribution of Ni, as well as the effect of the different remelt strategies (90° vs 67° rotation) examined.

The width of the Ni concentration distribution present in the microstructure narrows from 0 to 6 remelts, as each remelting step undergoes additional mixing (Fig. 5a-g). This is shown in the statistical variance of the compositions measured experimentally (Fig. 5h). The variances of Ni concentration are calculated using: Variance = $\sum_{i=0}^n p_i \times (X_i^{Ni} - X_{average}^{Ni})^2$. The change in remelt scan rotation (90° vs 67° rotation, Fig. 1) appears to have little effect on the Ni distribution, with the horizontal translation between the curves lying within the error margin of the measurements.

4. Discussion

The remelting steps applied to the 22Cr-6Ni mixed powder build show an evolution in melt pool size (Fig. 2), phase fractions and distributions (Fig. 3), grain morphology (Fig. 3) and chemical composition (Fig. 5), highlighting that remelting can be used as a tool for microstructural control if its effect on chemical homogeneity can be predicted. To understand how the number of remelts affects the chemical distribution, a model is required to connect the distributions of local chemistries to the physical process of remelting.

LPBF melting and remelting can be conceptually decomposed into a number of steps as shown in Fig. 6. In previous work [66], a model was presented to describe the chemistry distribution of as-built 22Cr-6Ni, based on single melting and mixing of particles. This model is extended here to the case of remelting. For the purposes of clarity, the key ingredients of this previous model [66] are revisited below.

The model assumes that the mixed 22Cr-6Ni powder is randomly distributed. This is thought to be a good approximation since the 22Cr powder and pure Ni powder have similar particle sizes and densities (Table 1). During a laser traverse, there is a probability, P, that k minority powder particles (pure Ni) are captured by the melt pool. This probability is expressed by a Poisson distribution, Eq. (1):

$$P(x=k) = \frac{\lambda^k e^{-\lambda}}{k!} \quad (1)$$

k = 0 refers to zero Ni particles being captured in the melt pool, k = 1 corresponds to 1 Ni particle being captured, etc... λ is the mean frequency of particle capture, calculated from the known overall composition of the powder mixture. The model assumes dissolution and complete mixing in the melt pool.

The model considers two printing process effects on the melt pool chemistry: partial scan track overlap in the same layer during printing and a remelting of the substrate during printing of successive layers (Fig. 6a). The quantity describing the number of Ni particles in a melt pool resulting from adjacent scan track overlap is the convolution of the probability distribution P (Eq. (1)) with itself, Eq. (2):

$$Q(x=k) = P * P = \frac{(2\lambda)^k e^{-(2\lambda)}}{k!} \quad (2)$$

* is the mathematical function for the convolution.

The quantity describing the number of Ni particles in a melt pool resulting from the mixing due to substrate remelting is the convolution of Q (Eq. (2)) with itself, Eq. (3):

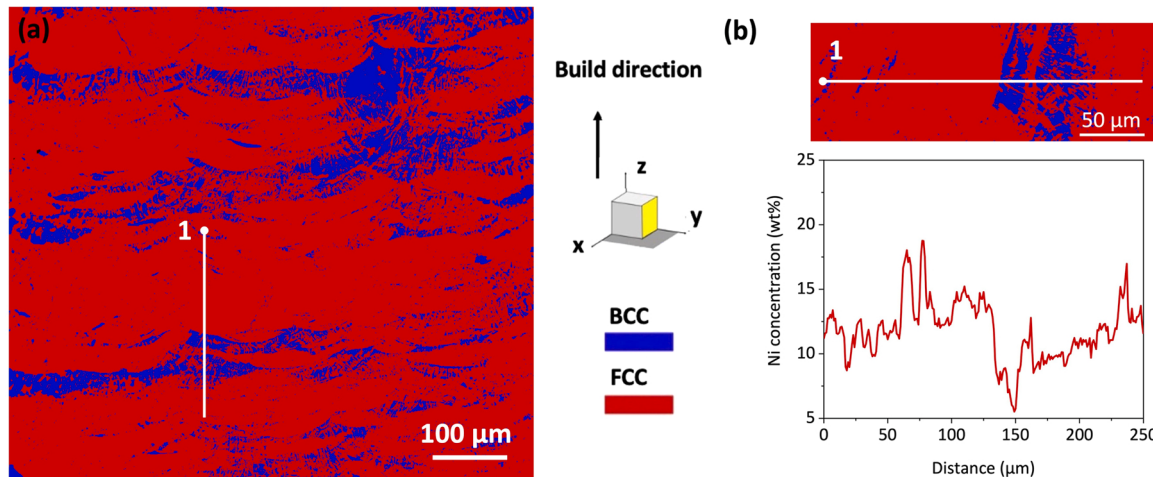


Fig. 4. EDS line scan across FCC and BCC regions in the 22Cr-6Ni after 1 remelt using the 90°-rotation remelting strategy: (a) phase identification map showing FCC (red) and BCC (blue) phase and the position of EDS line scan and (b) the Ni concentration along the line indicated in a).

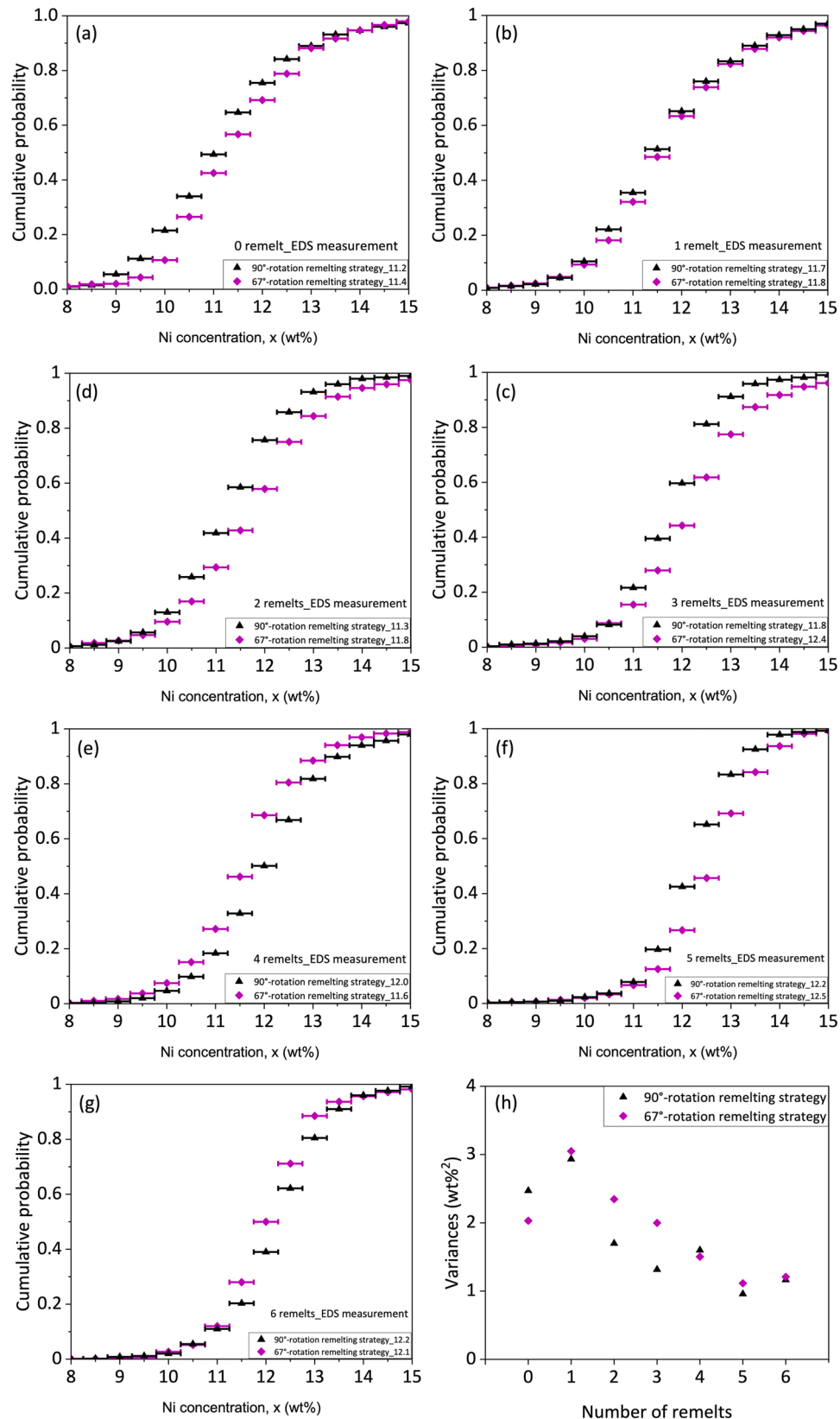


Fig. 5. (a)-(h) Effect of 0–6 remelts on the probability distribution for Ni EDS measurements in the 22Cr-6Ni samples printed using LPBF. The black dots refer to the EDS measurement from the 90°-rotation remelting strategy and the magenta dots refer to the EDS measurement from the 67°-rotation remelting strategy. The error bar represents the bin width for the EDS measurements (0.5 wt% Ni). (h) The variance of the chemical distribution for the 0–6 remelt samples from (a)-(g).

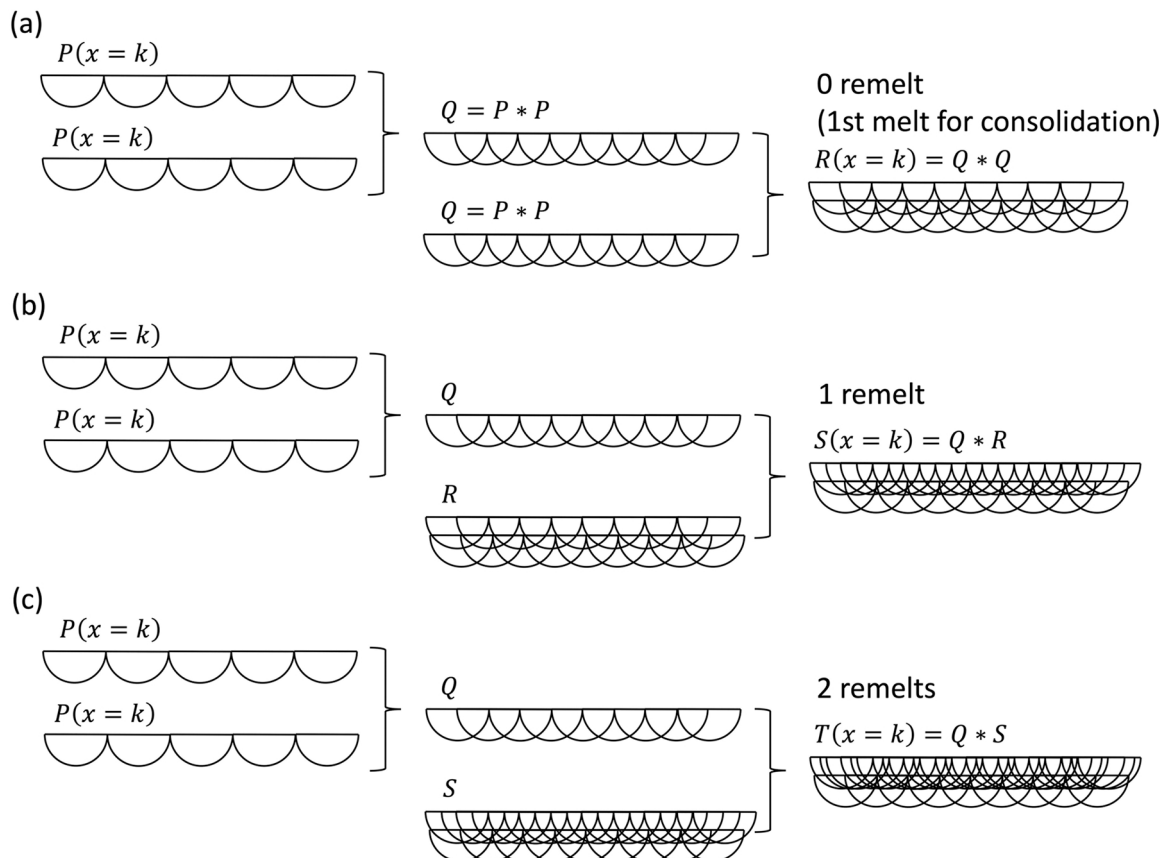


Fig. 6. Schematic illustration showing the deconvolution of melting and remelting process for the model. (a) 0 remelt for consolidation, (b) 1 remelt and (c) 2 remelts.

$$R(x=k) = Q * Q = \frac{(4\lambda)^k e^{-(4\lambda)}}{k!} \quad (3)$$

R represents the probability distribution for the number of Ni particles in the fully consolidated build assuming the starting state is a random powder mixture, Fig. 6a. The ability of this model to describe the experimental chemistry distribution in a mixed powder build has been demonstrated by Li et al. [66].

This model is now extended to describe the compositional distribution resulting from remelting. Again, two overlap effects must be considered during remelting: a) between neighbouring melt pools due to scan track overlap, and b) between successive layers due to remelting of the substrate layer. Both overlap effects contribute to compositional mixing during remelting. In the case of remelting, one must respect that the overlap of successive layers is occurring between two already consolidated layers, rather than a consolidated layer and a fresh powder layer.

During the remelting process, the probability distribution which describes the previous layer is the probability resulting from the previous melt/remelt. Fig. 6b and c show schematic illustrations for the processes corresponding to 1 remelt and 2 remelts. The probability distribution for the number of captured particles after 1 remelt, $S(x=k)$, is the convolution of Q and R (Fig. 6b), since R describes the probability distribution in the as-printed state. The probability distribution after 2 remelts, $T(x=k)$, is the convolution of Q and S (Fig. 6c). The probability distribution after n remelts ($n = 0, 1, 2, \text{etc.}$) can then be generalised, Table 2.

The variance of the probability distribution of the chemistry resulting from the printing of mixed powders can be used as a measure of compositional dispersion, representing how homogenous the composition becomes after n remelts ($n = 0, 1, 2, \text{etc.}$). Since the probability

Table 2
Probability distribution of captured particles in a melt pool during remelting.

Alloys	Probability distribution	Equation number
0 remelt	$R(x=k) = Q * Q = \frac{(4\lambda)^k e^{-(4\lambda)}}{k!}$	(3)
1 remelt	$S(x=k) = Q * R = \frac{[(4+2 \times 1) \bullet \lambda] \bullet e^{-[(4+2 \times 1) \bullet \lambda]}}{k!}$	(4)
2 remelts	$T(x=k) = Q * S = \frac{[(4+2 \times 2) \bullet \lambda] \bullet e^{-[(4+2 \times 2) \bullet \lambda]}}{k!}$	(5)
3 remelts	$U(x=k) = Q * T = \frac{[(4+2 \times 3) \bullet \lambda] \bullet e^{-[(4+2 \times 3) \bullet \lambda]}}{k!}$	(6)
4 remelts	$V(x=k) = Q * U = \frac{[(4+2 \times 4) \bullet \lambda] \bullet e^{-[(4+2 \times 4) \bullet \lambda]}}{k!}$	(7)
5 remelts	$W(x=k) = Q * V = \frac{[(4+2 \times 5) \bullet \lambda] \bullet e^{-[(4+2 \times 5) \bullet \lambda]}}{k!}$	(8)
6 remelts	$Y(x=k) = Q * W = \frac{[(4+2 \times 6) \bullet \lambda] \bullet e^{-[(4+2 \times 6) \bullet \lambda]}}{k!}$	(9)
n remelts	$Z(x=k) = \frac{[(4+2n) \bullet \lambda] \bullet e^{-[(4+2n) \bullet \lambda]}}{k!}$	(10)

distributions describing n remelts are Poisson distributions (resulting from Poisson distributions convoluted with themselves), the variance for n remelts is expressed as Eq. (11).

$$\text{Variance}(x=k) = \frac{\lambda}{4 + 2n} \quad (11)$$

The probability distribution of captured particles in a melt pool from a random powder mixture after n remelts ($n = 0, 1, 2, \text{etc.}$) and its variances, can then be converted to composition distributions using the known starting powder compositions.

The mixed powder of 22Cr-6Ni is used as a demonstration of this remelting model.

The mean frequency of particle capture, λ , describes the average number of Ni particles captured in a melt pool and depends on the melt pool size (Fig. 2d). Using the mass balance ($\sum_{i=1}^n p_i X_i^{Ni} = X_{bulk}^{Ni}$), $\lambda = 4.8$. The discrete probability distributions (Q, S, T, U, V, W , and Y), calculated using Eqs. (3)–(10), are shown in Fig. 7a. The variances calculated using Eq. (11) are shown in Fig. 7c. Fig. 7b and d show the corresponding predicted melt pool compositions and variances. As expected, $Q(x)$ is broader than $S(x)$ which is broader than $T(x)$. As more remelts occur, the probability distribution of the composition in the melt pools becomes narrower.

A test of the predictions of $Q(x), S(x), T(x), U(x), V(x), W(x)$, and $Y(x)$ for 0–6 remelts (Eqs. (3)–(10) and Fig. 7b) is to compare the predicted chemical distributions with the EDS measurements of the chemical compositions (Fig. 5). Since the 90°-rotation remelting strategy and the 67°-rotation remelting strategy showed equivalent effects on the homogeneity (Fig. 5), the results of the 90°-rotation remelting strategy are used for the comparisons below. The distributions in Fig. 7b were converted to cumulative probability distributions to compare with the EDS compositions shown in Fig. 5.

Two model curves and the experimental EDS measurements, are compared in Fig. 8. The black curve assumes the mixed powder has an average Ni content of 11.2 wt% (Table 1, from the mass balance), whereas the orange curve uses the average Ni concentration obtained from the experimental EDS measurements. The average composition of the initial powder mixture and the average composition measured from EDS should be exactly the same but they can differ due to evaporation effects during printing. Small variations in the average Ni concentration

can induce a horizontal translation between the two model curves, especially for 3–6 remelts, but has little effect on the shape. When the number of remelts is greater than 3, the horizontal translation can reach up to 1.0 wt%. To confirm the translation observed is due to elemental evaporation, the EDS measurements for Ni, Mo, Fe, Cr, Mn, and Si over the 6 remelt scans, are shown in Fig. 9a-f. The red line in each plot represents the initial content of each element in the mixed 22Cr-6Ni powder (Table 1). As the process of remelting occurs, the contents of Ni and Mo increase while the contents of Cr and Mn decrease. The increase of Ni and Mo content is approximately equal to the decrease of Cr and Mn, as shown in Fig. 9g. This demonstrates that the transition between the two model curves in Fig. 8a-g is due to the preferential evaporation of the Cr and Mn during the remelting process.

In addition to monitoring changes in the substitutional elements during remelting, the nitrogen content has also been measured by LECO combustion (with precision of ± 0.02 wt%) after each step of remelting and is shown in Fig. 9h. Since the build is performed in a nitrogen atmosphere it is important to monitor for any nitrogen pick-up since nitrogen is an austenite (FCC) stabiliser. As shown in Fig. 9h, the nitrogen content does not show an statistically significant variation during remelting.

When the average Ni concentration measured using EDS is used to calculate λ , the model predicts the experimental data extremely well at 0 remelts. However, the model becomes less accurate as the number of remelts increases (Fig. 8e-g). This is especially clear in the tails of the distributions. The model predicts more mixing than is experimentally observed. One reason could be the reduction in melt pool size during

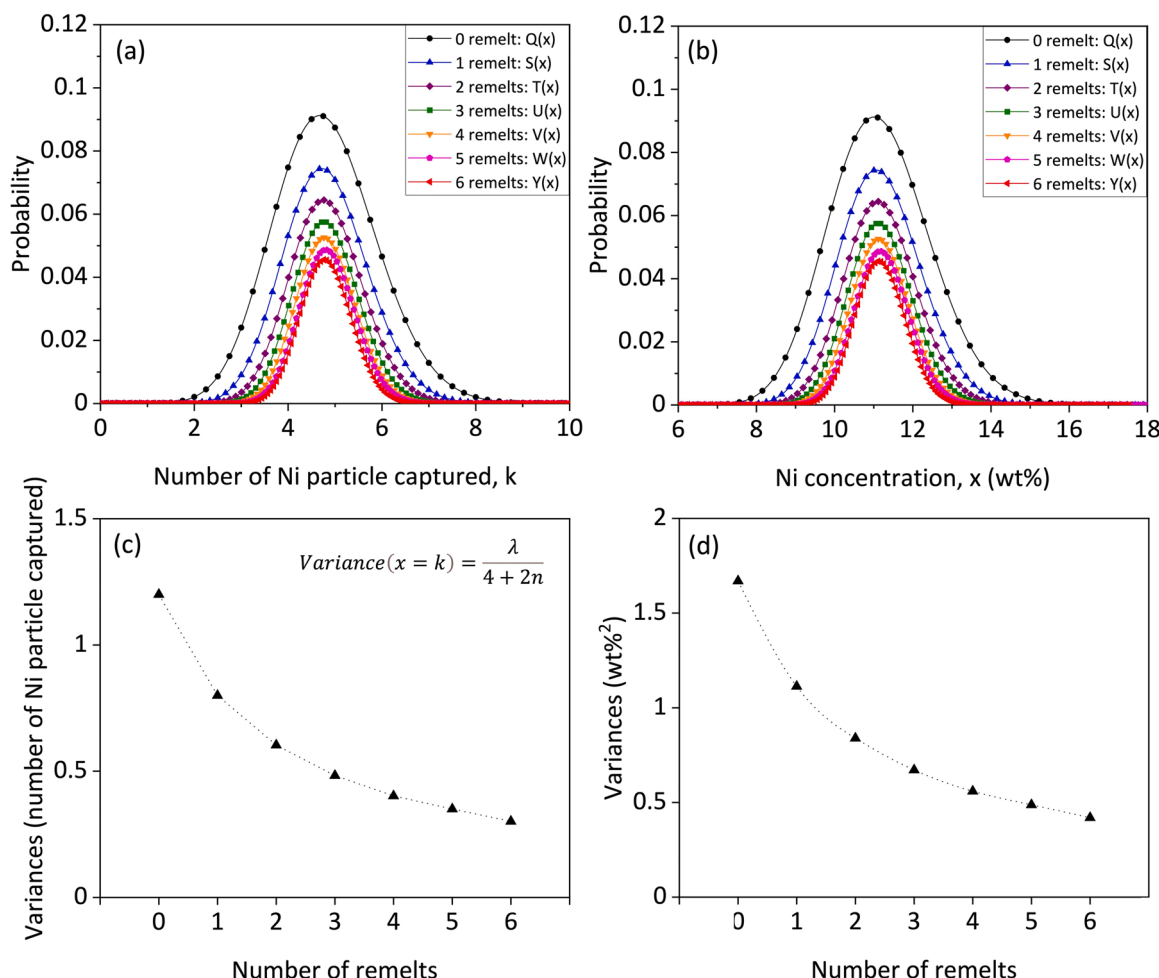


Fig. 7. (a) Discrete Poisson probability distribution of 0–6 remelts for the number of Ni particles captured in the powder mixture. (b) The probability distributions for Ni concentration calculated from (a). (c) and (d) are the comparisons of the variances in the terms of the number of Ni particles captured and Ni content.

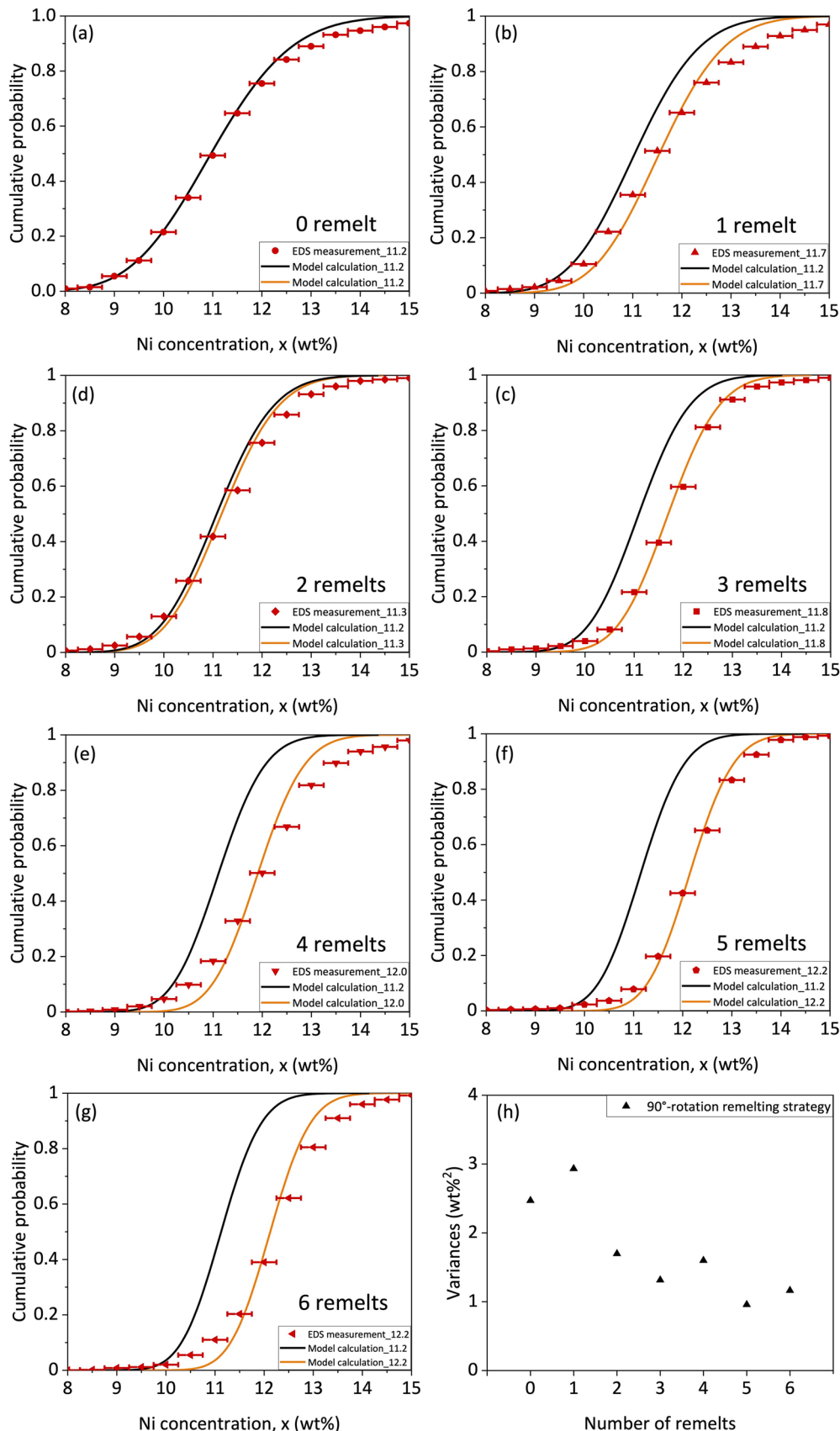


Fig. 8. (a)-(g) Model predictions compared with experimental EDS (red dots) measurements of Ni in the 22Cr-6Ni built using the 90°-rotation remelting strategy. The black curves correspond to the model using the average Ni content of 11.2 wt%, and the orange curves correspond to the model using the experimentally measured average Ni content. (h) The variances of 0–6 remelts from (a)–(g).

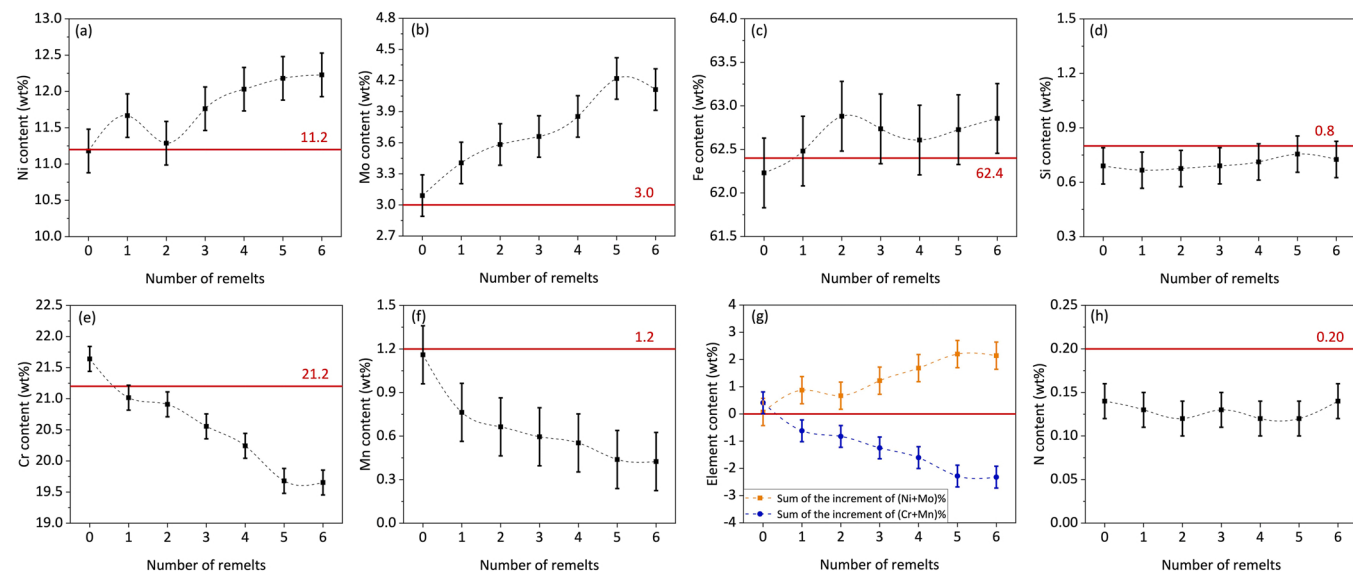


Fig. 9. The content of (a) Ni, (b) Mo, (c) Fe, (d) Si, (e) Cr and (f) Mn measured experimentally using EDS for 0–6 remelts in the 22Cr-6Ni built using the 90°-rotation remelting strategy. (g) Comparison between the sum of the increment of Ni and Mo content and the sum of the increment of Cr and Mn. (h) The corresponding content of nitrogen measured using LECO combustion analysis for 0–6 remelts.

remelting, as shown in Fig. 2d.

As shown in Fig. 2, the melt pool size decreases during remelting even though the process parameters (laser power, scanning speed, hatch distance, and layer thickness) are constant. This reduction in melt pool size during remelting has been previously reported and is attributed to the partial reflection of the laser energy by the already consolidated surface [70,71]. Smaller melt pools result in a smaller volume of material involved in mixing, which weakens the effect of remelting on compositional mixing. The effect of a smaller melt pool on the compositional distribution is then magnified with increasing remelts.

The effect of this decreasing melt pool size can be introduced into the model and these are shown as the blue curves in Fig. 10. The previous ‘constant melt pool’ model is shown in orange, and the EDS measurements are shown in red for different numbers of remelts. The orange curves assume a constant melt pool size and use the average experimental EDS measurement of Ni. They are consistent with the orange curves in Fig. 8. The blue curves use the average Ni concentration measured from EDS but with a melt pool size that varies as a function of the number of remelts, as shown in Fig. 2d. The agreement between the model (blue curves) and experimental EDS measurement is excellent. Taking elemental evaporation and the variation in melt pool size during remelting into consideration is important to predict the chemical homogeneity of the build. The model is also compared with the EDS measurements using the 67°-rotation remelting strategy data in Fig. 11, showing an equally good agreement.

5. Strategies to obtain chemically homogeneous builds using mixed powders

Previously, we have presented a model to predict the chemistry distribution in a mixed powder build [66]. This has now been extended to the case of remelting. This model should be capable of identifying the best strategies to minimise chemical heterogeneity for those interested in using mixed powders to examine new alloy compositions in LPBF.

The first strategy is to avoid using powders that have a much higher melting point than the average melting point of the powder mixture. These problems have already been observed many times when trying to in-situ alloy using refractory additions such as Mo, Nb, Ta [3–8,14,25, 27–32], etc. Remelting may assist by providing more time for dissolution of these high melting point powders but avoiding them in the first place is an obvious first strategy.

However, if we do print a powder mixture where all the powders do dissolve and mix in the melt pool, then the level of chemical heterogeneity obtained depends on the ratio of the melt pool size and the minority particle spacing. If the size of the melt pool is much larger than the minority particle spacing then each melt pool will capture a large number of minority particles and the chemical heterogeneity in the build will be lower. There are three ways to reduce the chemical heterogeneity in builds from mixed powders: increase the melt pool size, decrease the minority powder particle spacing, apply remelting.

For a given powder mixture, increasing the melt pool size will generally tend to benefit chemical homogeneity when measured at the mesoscale. Melt pool size can be increased by increasing the laser energy [14,38,58] or decreasing the scan speed [10,38,48,66]. Both approaches have been shown experimentally to improve homogeneity. One still needs to be able to print without printing defects (e.g. keyhole defects) and this provides constraints on the realistically achievable melt pool sizes. To provide a concrete example, Fig. 12a and b show the expected effect of changing the melt pool size for the powder mixture of 22Cr-6Ni used in this study. When the scanning speed is decreased, the melt pool size increases. A larger melt pool will capture more minority powder particles (pure Ni) resulting in a decrease in the statistical variance of the composition. Modest increases in the melt pool size can have significant effects on the chemical homogeneity. Fig. 12a and b demonstrate that for the example of 22Cr-6Ni mixture, an increase in the melt pool diameter from 160 to 200 μm leads to a decrease in the variance of the chemical distribution from 4 wt% to ~ 1.5 wt%.

Another method to improve the chemical homogeneity in the as-built state obtained from mixed powders is to reduce the minority particle spacing in the starting powder mixture. For a given overall powder mixture composition, this is achieved by reducing the minority powder particle size (i.e. there must be more particles, spaced closer together, to achieve the same composition as a few, larger, further spaced particles). The extreme case of this strategy is ‘satelliting’ where very small minority particles are attached to the majority powder particles. This has been reported in the literature with great success [1].

A danger with reducing the minority powder particle size compared to the majority powder particle size, is the risk of settling or clumping of the minority powder, and therefore moving away from the random powder representation which will lead to more chemical heterogeneity. Satelliting solves this problem by having the minority powder particles attached to the major powder particles. To quantitatively demonstrate

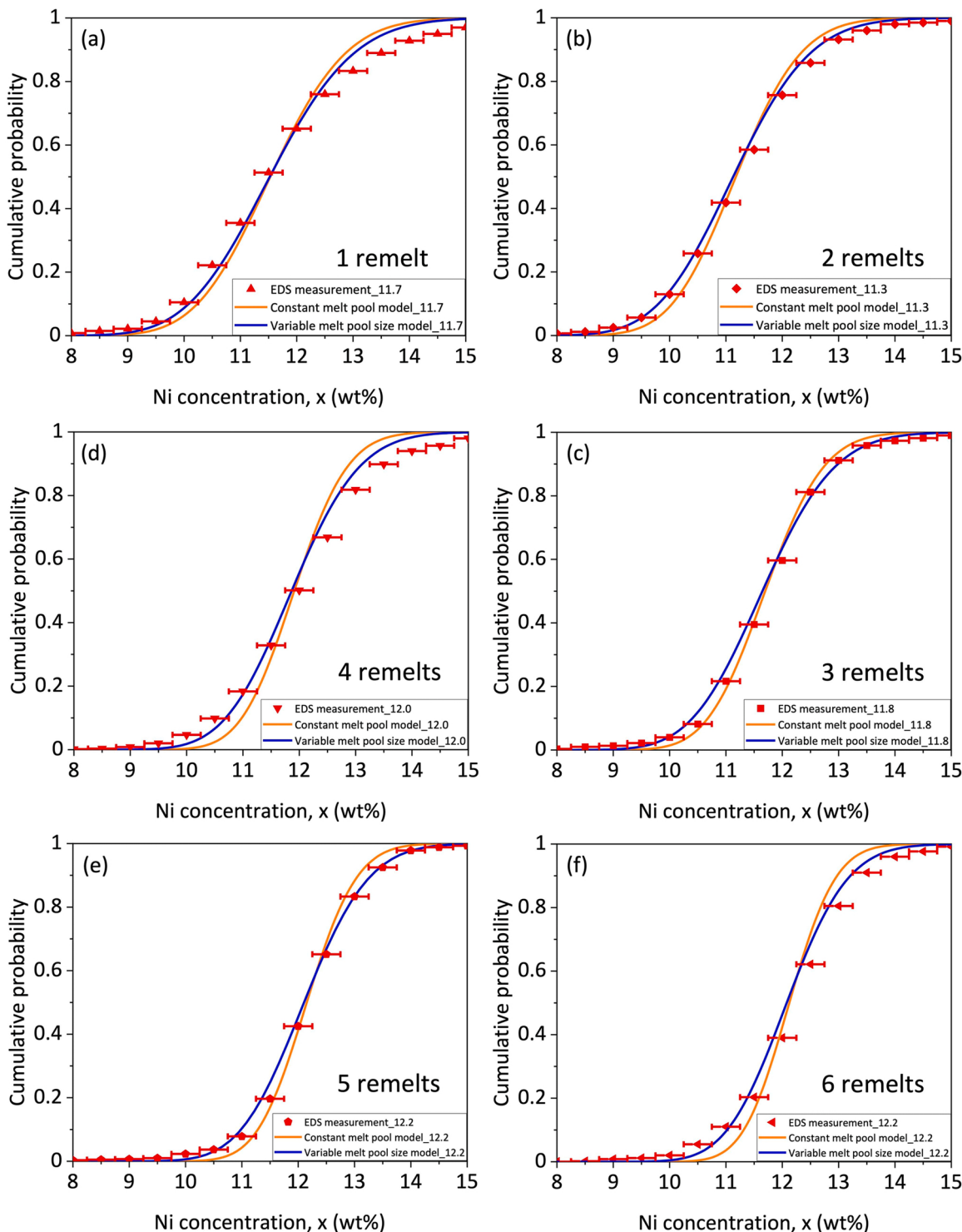


Fig. 10. (a)-(f) Model predictions compared with Ni measured experimentally using EDS (red dots) in the 22Cr-6Ni built using the 90° rotation remelt strategy. The orange model curve assumes a constant melt pool size using the average Ni content measured using EDS, and the blue model curve takes into account the evolution of the melt pool size during remelting as shown in Fig. 2d.

the effect of reducing the minority powder particle size on the chemical homogeneity in the build, an example is shown in Fig. 12c and d. For a constant melt pool size, corresponding to a scanning speed of 300 mm/s using the 22Cr-6Ni powder, as the diameter of a minority powder particle is decreased (and therefore the number of particles increases, and their average spacing decreases), the probability of a melt pool capturing a minority powder particle is increased significantly. Correspondingly, the variance of the Ni concentration decreases with the

decrease of nickel powder particle size. This is potentially a large effect. In the example shown in Fig. 12, a decrease in the Ni powder particle size from 32 μm to 16 μm , leads to a decrease in the variance in the chemical distribution from ~ 4 wt% to ~ 1.5 wt%.

The third strategy that can be used to improve chemical homogeneity is remelting. The work presented in this contribution shows that indeed remelting is an effective means of reducing the chemical heterogeneity resulting from mixed powders but Fig. 8h demonstrates that the

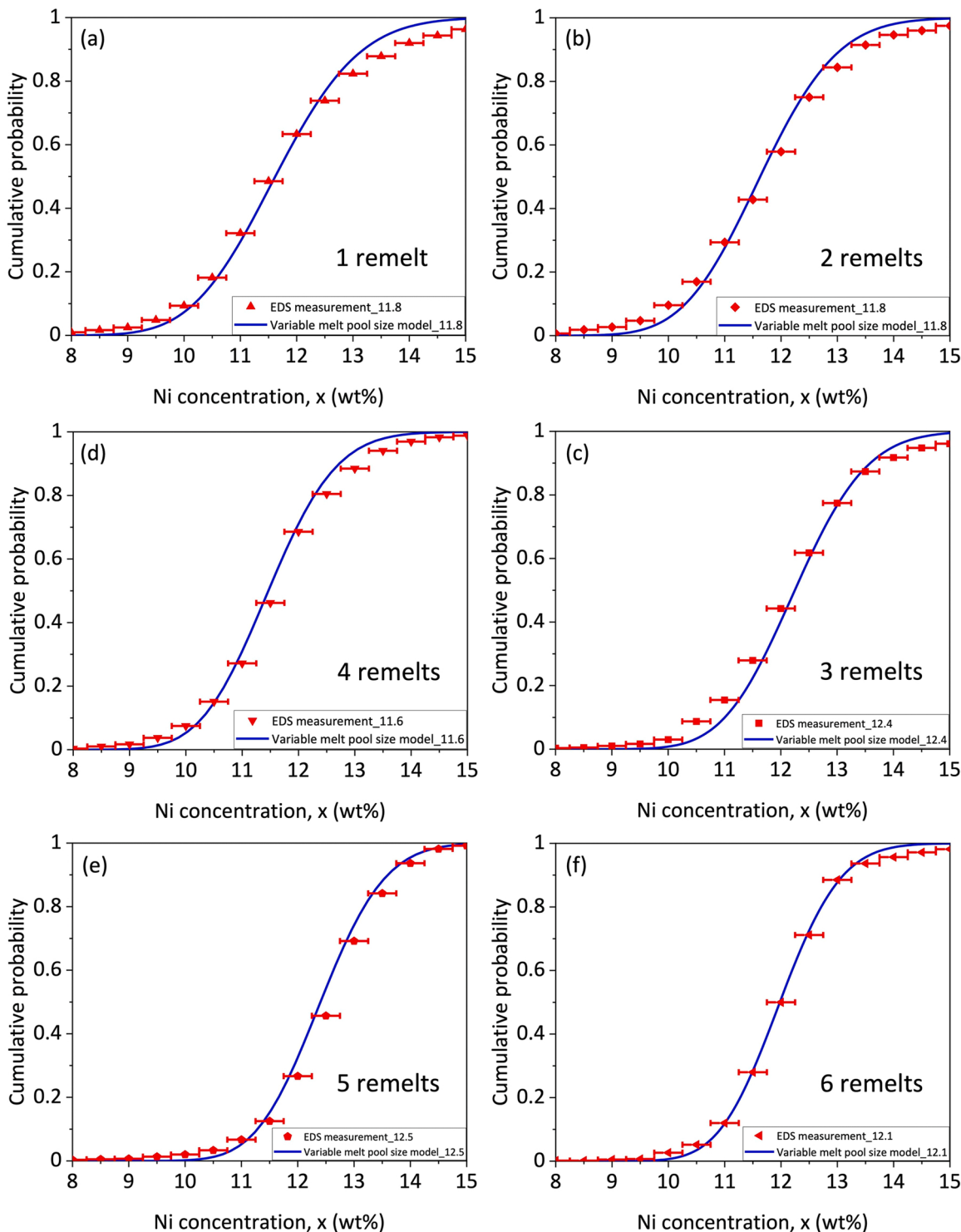


Fig. 11. (a)-(f) Model predictions compared with Ni measured experimentally using EDS (red dots) in the 22Cr-6Ni built using the 67° rotation remelt strategy. The blue model curve takes into account the evolution of the melt pool size during remelting as shown in Fig. 2d.

effectiveness of this approach decreases after 2–3 remelts. Remelting more than 3 times provides little additional benefit. The disadvantage of remelting is that it greatly increases the printing time and the melt pool will generally be smaller because of the reflectivity of the already solidified material and this further lessens the effectiveness.

However, remelting does have a very interesting advantage that has not been discussed in much depth yet in the literature. Since remelting can be spatially controlled and it can be used to modify the probability distribution of the local chemistry, and the phases that form during

solidification depend on the local chemistry, remelting can be used to spatially control phase formation at the mesoscale, opening the possibility for the fabrication of architected materials using LPBF.

Fig. 3 demonstrates experimentally that remelting can be used to control a transition from a FCC+BCC structure (Fig. 3a), to a fully FCC structure (Fig. 3d). There are two reasons for this transition – a) remelting narrows the probability distribution of the chemistry and shifts a larger fraction of the microstructure above the critical Ni content to trigger FCC formation from the liquid during solidification [66], and

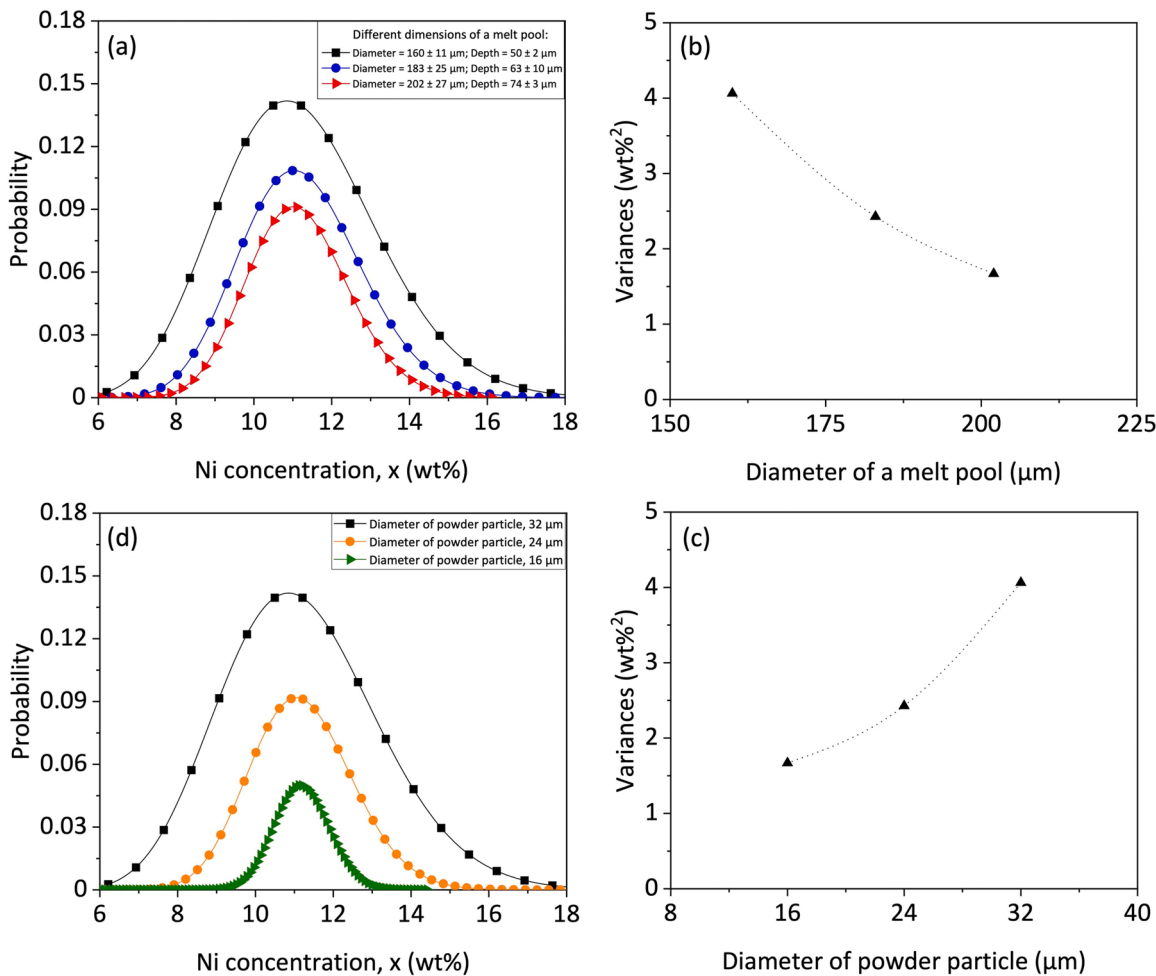


Fig. 12. (a) and (b) are the probability distributions for the Ni concentration from the model calculation and the corresponding variances in the 22Cr-6Ni powder mixture for different melt pool sizes. (c) and (d) are the probability distributions for the Ni concentration from the model calculation and the corresponding variances using a constant melt pool size for different minority (pure Ni) powder particle sizes.

b) evaporation of some elements during remelting leads to a shift of the average Ni content of the build to higher values (horizontal shift of the orange curve compared to the black curve in Fig. 8). Fig. 13 below shows an example where spatially controlled remelting has been used for

mesoscale phase control to create a layered pattern of FCC+BCC and fully FCC. Since remelting is spatially controlled, any type of mesoscale pattern is possible. This provides an interesting new path for the fabrication of architected materials using LPBF.

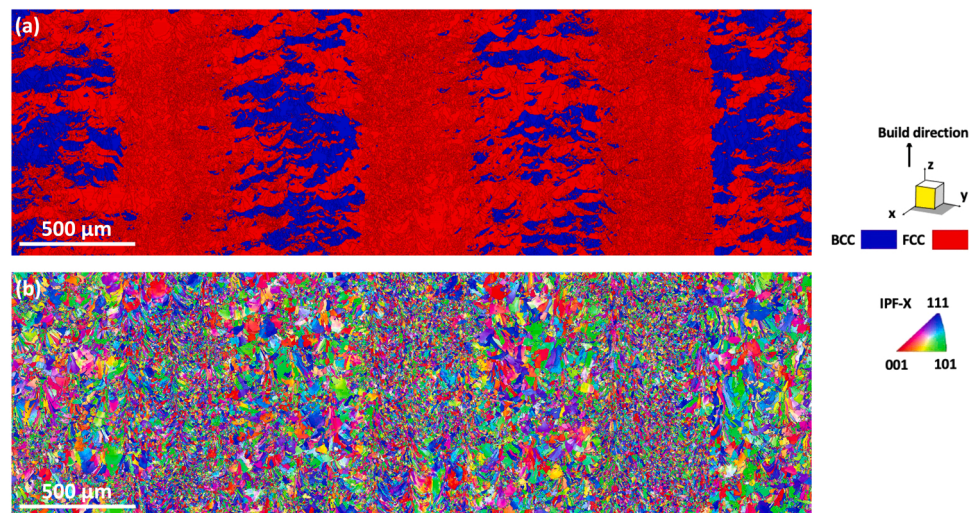


Fig. 13. Phase identification map (a) and inverse pole figure map (b) for a fully FCC stripe-patterned architected steels. The designed width of the fully FCC stripe is 0.5 mm and the distance between two stripes and is 0.5 mm. The fully FCC stripe regions were remelted 6 times.

6. Conclusion

A model to describe the chemistry distribution resulting from LPBF of mixed powders is presented with specific application to remelting. The predictions are compared with experimental measurements showing excellent agreement so long as evaporation effects are included and the decrease in melt pool size during remelting is respected. The key factors in promoting chemical homogeneity when printing physically mixed powders using LPBF are discussed and the possibility of using spatially controlled remelting of physically mixed powders to provide mesoscale control of phase formation is shown. The latter provides an interesting new path to the fabrication of architected materials using LPBF.

CRediT authorship contribution statement

Huikai Li: Writing – review & editing, Writing – original draft, Visualization, Validation, Investigation, Formal analysis, Data curation. **Erin G. Brodie:** Writing – review & editing, Validation, Supervision, Project administration, Methodology, Investigation, Formal analysis, Conceptualization. **Christopher Hutchinson:** Writing – review & editing, Supervision, Resources, Project administration, Methodology, Investigation, Funding acquisition, Formal analysis, Conceptualization.

Declaration of Competing Interest

The authors declare that they have no known competing financial interests or personal relationships that could have appeared to influence the work reported in this paper.

Data availability

Data will be made available on request.

Acknowledgements

Huikai Li acknowledges Monash University for the award of a Ph.D. scholarship (FEIPRS & MDS). This work was supported by Woodside Energy and the Australian Research Council in the form of a Linkage Project (LP160100918), and by the Woodside Energy FutureLab at Monash University. The authors would also like to express thanks for the use of equipment within the Monash Centre for Electron Microscopy (MCEM) and the Monash X-Ray Platform (MXP).

References

- [1] M.H. Mosallanejad, B. Niroumand, A. Aversa, A. Saboori, In-situ alloying in laser-based additive manufacturing processes: a critical review, *J. Alloy. Compd.* 872 (2021), 159567.
- [2] M. Simonelli, N.T. Aboulkhair, P. Cohen, J.W. Murray, A.T. Clare, C. Tuck, R.J. M. Hague, A comparison of Ti-6Al-4V in-situ alloying in selective laser melting using simply-mixed and satellited powder blend feedstocks, *Mater. Charact.* 143 (2018) 118–126.
- [3] B. Vrancken, L. Thijss, J. Kruth, J. Van Humbeeck, Microstructure and mechanical properties of a novel β titanium metallic composite by selective laser melting, *Acta Mater.* 68 (2014) 150–158.
- [4] L.L. Xing, C.C. Zhao, H. Chen, Z.J. Shen, W. Liu, Microstructure of a Ti-50 wt% Ta alloy produced via laser powder bed fusion, *Acta Metall. Sin. Engl. Lett.* 33 (2020) 981–990.
- [5] E.G. Brodie, J. Richter, T. Wegener, T. Niendorf, A. Molotnikov, Low-cycle fatigue performance of remelted laser powder bed fusion (L-PBF) biomedical Ti25Ta, *Mater. Sci. Eng. A* 798 (2020), 140228.
- [6] E.G. Brodie, A.E. Medvedev, J.E. Frith, M.S. Dargusch, H.L. Fraser, A. Molotnikov, Remelt processing and microstructure of selective laser melted Ti25Ta, *J. Alloy. Compd.* 820 (2020), 153082.
- [7] P. Qin, L.Y. Chen, C.H. Zhao, Y.J. Liu, C.D. Cao, H. Sun, L.C. Zhang, Corrosion behavior and mechanism of selective laser melted Ti35Nb alloy produced using pre-alloyed and mixed powder in Hank's solution, *Corros. Sci.* 189 (2021), 109609.
- [8] N. Soro, E.G. Brodie, A. Abdal-hay, A.Q. Alali, D. Kent, M.S. Dargusch, Additive manufacturing of biomimetic titanium-tantalum lattices for biomedical implant applications, *Mater. Des.* 218 (2022), 110688.
- [9] K. Zhuravleva, M. Bönisch, K.G. Prashanth, U. Hempel, A. Helth, T. Gemming, M. Calin, S. Scudino, L. Schultz, J. Eckert, A. Gebert, Production of porous β -type Ti-40Nb alloy for biomedical applications: comparison of selective laser melting and hot pressing, *Materials* 6 (2013) 5700–5712.
- [10] B. Zhang, J. Chen, C. Coddet, Microstructure and transformation behavior of in-situ shape memory alloys by selective laser melting Ti-Ni mixed Powder, *J. Mater. Sci. Technol.* 29 (2013) 863–867.
- [11] S. Shiva, I.A. Palani, S.K. Mishra, C.P. Paul, L.M. Kukreja, Investigations on the influence of composition in the development of Ni-Ti shape memory alloy using laser based additive manufacturing, *Opt. Laser Technol.* 69 (2015) 44–51.
- [12] C. Qiu, A. Fones, H.G.C. Hamilton, N.J.E. Adkins, M.M. Attallah, A new approach to develop palladium-modified Ti-based alloys for biomedical applications, *Mater. Des.* 109 (2016) 98–111.
- [13] L. Yan, Y. Yuan, L. Ouyang, H. Li, A. Mirzasadeghi, L. Li, Improved mechanical properties of the new Ti-15Ta-xZr alloys fabricated by selective laser melting for biomedical application, *J. Alloy. Compd.* 688 (2016) 156–162.
- [14] M. Fischer, D. Jouquet, G. Robin, L. Peltier, P. Laheurte, In situ elaboration of a binary Ti-26Nb alloy by selective laser melting of elemental titanium and niobium mixed powders, *Mater. Sci. Eng. C* 62 (2016) 852–859.
- [15] Q. Wang, C. Han, T. Choma, Q. Wei, C. Yan, B. Song, Y. Shi, Effect of Nb content on microstructure, property and in vitro apatite-forming capability of Ti-Nb alloys fabricated via selective laser melting, *Mater. Des.* 126 (2017) 268–277.
- [16] S. Guo, Y. Lu, S. Wu, L. Liu, M. He, C. Zhao, Y. Gan, J. Lin, J. Luo, X. Xu, J. Lin, Preliminary study on the corrosion resistance, antibacterial activity and cytotoxicity of selective-laser-melted Ti6Al4V-xCu alloys, *Mater. Sci. Eng. C* 72 (2017) 631–640.
- [17] M. Todai, T. Nagase, T. Hori, H. Motoki, S.H. Sun, K. Hagihara, T. Nakano, Fabrication of the beta-titanium alloy rods from a mixture of pure metallic element powders via selected laser melting, *Mater. Sci. Forum* 94 (2018) 1260–1263.
- [18] S. Huang, S.L. Sing, W.Y. Yeong, Selective laser melting of Ti42Nb composite powder and the effect of laser re-melting, *Key Eng. Mater.* 801 (2019) 270–275.
- [19] T. Nagase, T. Hori, M. Todai, S.H. Sun, T. Nakano, Additive manufacturing of dense components in beta-titanium alloys with crystallographic texture from a mixture of pure metallic element powders, *Mater. Des.* 173 (2019), 107771.
- [20] C. Zhao, H. Liang, S. Luo, J. Yang, Z. Wang, The effect of energy input on reaction, phase transition and shape memory effect of NiT alloy by selective laser melting, *J. Alloy. Compd.* 817 (2020), 153288.
- [21] D. Zhao, C. Han, J. Li, J. Liu, Q. Wei, In situ fabrication of a titanium-niobium alloy with tailored microstructures, enhanced mechanical properties and biocompatibility by using selective laser melting, *Mater. Sci. Eng. C* 111 (2020), 110784.
- [22] N. Kang, X. Lin, C. Coddet, X. Wen, W. Huang, Selective laser melting of low modulus Ti-Mo alloy: α/β heterogeneous conchoidal structure, *Mater. Lett.* 267 (2020), 127544.
- [23] T. Zhang, Z. Huang, T. Yang, H. Kong, J. Luan, A. Wang, D. Wang, W. Kuo, Y. Wang, C.-T. Liu, In situ design of advanced titanium alloy with concentration modulations by additive manufacturing, *Science* 374 (2021) 478–482.
- [24] F.F. Ahmed, S.J. Clark, C.L. Alex Leung, L. Stanger, J. Willmott, S. Marussi, V. Honkimaki, N. Haynes, H.S. Zurob, P.D. Lee, A.B. Phillion, Achieving homogeneity in a high-Fe β -Ti alloy laser-printed from blended elemental powders, *Mater. Des.* 210 (2021), 110072.
- [25] S.L. Sing, W.Y. Yeong, F.E. Wiria, Selective laser melting of titanium alloy with 50 wt% tantalum: microstructure and mechanical properties, *J. Alloy. Compd.* 660 (2016) 461–470.
- [26] Y.P. Dong, Y.L. Li, S.Y. Zhou, Y.H. Zhou, M.S. Dargusch, H.X. Peng, M. Yan, Cost-affordable Ti-6Al-4V for additive manufacturing: powder modification, compositional modulation and laser in-situ alloying, *Addit. Manuf.* 37 (2021), 101699.
- [27] I. Yadroitsev, P. Krakhmalev, I. Yadroitseva, Titanium alloys manufactured by in situ alloying during laser powder bed fusion, *JOM* 69 (2017) 2725–2730.
- [28] A. Grigoriev, I. Polozov, V. Sufiarov, A. Popovich, In-situ synthesis of Ti2AlNb-based intermetallic alloy by selective laser melting, *J. Alloy. Compd.* 704 (2017) 434–442.
- [29] I. Polozov, V. Sufiarov, A. Popovich, D. Masaylo, A. Grigoriev, Synthesis of Ti-5Al, Ti-6Al-7Nb, and Ti-22Al-25Nb alloys from elemental powders using powder-bed fusion additive manufacturing, *J. Alloy. Compd.* 763 (2018) 436–445.
- [30] J.C. Wang, Y.J. Liu, P. Qin, S.X. Liang, T.B. Sercombe, L.C. Zhang, Selective laser melting of Ti-35Nb composite from elemental powder mixture: microstructure, mechanical behavior and corrosion behavior, *Mater. Sci. Eng. A* 760 (2019) 214–224.
- [31] N. Soro, H. Attar, E. Brodie, M. Veidt, A. Molotnikov, M.S. Dargusch, Evaluation of the mechanical compatibility of additively manufactured porous Ti-25Ta alloy for load-bearing implant applications, *J. Mech. Behav. Biomed. Mater.* 97 (2019) 149–158.
- [32] Q. Sui, L. Meng, S. Wang, P. Li, X. Yin, L. Wang, Effect of Nb addition on mechanical properties and corrosion behavior of Ti6Al4V alloy produced by selective laser melting, *J. Mater. Res.* 35 (2020) 571–579.
- [33] C. Shuai, C. He, Z. Dong, Y. Yang, S. Peng, W. Tan, Galvanic corrosion induced by heterogeneous bimodal grain structures in Fe-Mn implant, *Mater. Charact.* 180 (2021), 111445.
- [34] M.L. Köhler, J. Kunz, S. Herzog, A. Kaletsch, C. Broeckmann, Microstructure analysis of novel LPBF-processed duplex stainless steels correlated to their mechanical and corrosion properties, *Mater. Sci. Eng. A* 801 (2021), 140432.
- [35] C. Donik, J. Kraner, A. Kocijan, I. Paulin, M. Godec, Evolution of the ϵ and γ phases in biodegradable Fe-Mn alloys produced using laser powder-bed fusion, *Sci. Rep.* 11 (2021) 19506.

- [36] Y. Guo, M.C. Zhao, B. Xie, Y.C. Zhao, D. Yin, C. Gao, C. Shuai, A. Atrens, In vitro corrosion resistance and antibacterial performance of novel Fe–xCu biomedical alloys prepared by selective laser melting, *Adv. Eng. Mater.* 23 (2021) 1–14.
- [37] J. Kraner, J. Medved, M. Godec, I. Paulin, Thermodynamic behavior of Fe-Mn and Fe-Mn-Ag powder mixtures during selective laser melting, *Metals* 11 (2021) 1–12.
- [38] P. Chen, S. Li, Y. Zhou, M. Yan, M.M. Attallah, Fabricating CoCrFeMnNi high entropy alloy via selective laser melting in-situ alloying, *J. Mater. Sci. Technol.* 43 (2020) 40–43.
- [39] Y. Hou, H. Su, H. Zhang, X. Wang, C. Wang, Fabricating homogeneous fecocrni high-entropy alloys via slm in situ alloying, *Metals* 11 (2021) 942, <https://doi.org/10.3390/met11060942>.
- [40] J. Gao, Y. Jin, Y. Fan, D. Xu, L. Meng, C. Wang, Y. Yu, D. Zhang, F. Wang, Fabricating antibacterial CoCrCuFeNi high-entropy alloy via selective laser melting and in-situ alloying, *J. Mater. Sci. Technol.* 102 (2022) 159–165.
- [41] M.S. Knieps, W.J. Reynolds, J. Dejaune, A.T. Clare, A. Evrigen, In-situ alloying in powder bed fusion: the role of powder morphology, *Mater. Sci. Eng. A* 807 (2021), 140849.
- [42] A. El Hassanin, F. Scherillo, U. Prisco, R. Sansone, A. Astarita, Selective laser melting of Cu-inconel 718 powder mixtures, *J. Manuf. Process.* 59 (2020) 679–689.
- [43] A. Chmielewska, B. Wysocki, J. Buhagiar, B. Michalski, B. Adamczyk-Cieślak, M. Gloc, W. Święszkowski, In situ alloying of NiTi: Influence of laser powder bed fusion (LBPF) scanning strategy on chemical composition, *Mater. Today Commun.* 30 (2022), 103007.
- [44] A. El Hassanin, A.T. Silvestri, F. Napolitano, F. Scherillo, A. Caraviello, D. Borrelli, A. Astarita, Laser-powder bed fusion of pre-mixed Inconel718-Cu powders: an experimental study, *J. Manuf. Process.* 71 (2021) 329–344.
- [45] Y. Wen, B. Zhang, R.L. Narayan, P. Wang, X. Song, H. Zhao, U. Ramamurty, X. Qu, Laser powder bed fusion of compositionally graded CoCrMo-Inconel 718, *Addit. Manuf.* 40 (2021), 101926.
- [46] R. Zhao, T. Yang, H. Liao, N. Fenineche, C. Coddet, J. Gao, Nanoscale chemistry and atomic-scale microstructure of a bulk Ni3Sn material built using selective laser melting of elemental powder blends, *Mater. Des.* 211 (2021), 110152.
- [47] G. Marchese, M. Beretta, A. Aversa, S. Biamino, In situ alloying of a modified inconel 625 via laser powder bed fusion: microstructure and mechanical properties, *Metals* 11 (2021) 988.
- [48] R. Zhao, J. Gao, H. Liao, N. Fenineche, C. Coddet, Selective laser melting of elemental powder blends for fabrication of homogeneous bulk material of near-eutectic Ni–Sn composition, *Addit. Manuf.* 34 (2020), 101261.
- [49] K. Wei, X. Zeng, Z. Wang, J. Deng, M. Liu, G. Huang, X. Yuan, Selective laser melting of Mg-Zn binary alloys: effects of Zn content on densification behavior, microstructure, and mechanical property, *Mater. Sci. Eng. A* 756 (2019) 226–236.
- [50] C. Shuai, L. Liu, M. Zhao, P. Feng, Y. Yang, W. Guo, C. Gao, F. Yuan, Microstructure, biodegradation, antibacterial and mechanical properties of ZK60-Cu alloys prepared by selective laser melting technique, *J. Mater. Sci. Technol.* 34 (2018) 1944–1952.
- [51] C. Shuai, Y. Yang, S. Peng, C. Gao, P. Feng, J. Chen, Y. Liu, X. Lin, S. Yang, F. Yuan, Nd-induced honeycomb structure of intermetallic phase enhances the corrosion resistance of Mg alloys for bone implants, *J. Mater. Sci. Mater. Med.* 28 (2017) 1–12.
- [52] X. Niu, H. Shen, J. Fu, Microstructure and mechanical properties of selective laser melted Mg-9 wt%Al powder mixture, *Mater. Lett.* 221 (2018) 4–7.
- [53] J.A. Glerum, C. Kenel, T. Sun, D.C. Dunand, Synthesis of precipitation-strengthened Al-Sc, Al-Zr and Al-Sc-Zr alloys via selective laser melting of elemental powder blends, *Addit. Manuf.* 36 (2020), 101461.
- [54] N. Kang, P. Coddet, L. Dembinski, H. Liao, C. Coddet, Microstructure and strength analysis of eutectic Al-Si alloy in-situ manufactured using selective laser melting from elemental powder mixture, *J. Alloy. Compd.* 691 (2017) 316–322.
- [55] R. Martinez, I. Todd, K. Mumtaz, In situ alloying of elemental Al-Cu12 feedstock using selective laser melting, *Virtual Phys. Prototyp.* 14 (2019) 242–252.
- [56] M.L. Montero Sistiaga, R. Mertens, B. Vrancken, X. Wang, B. Van Hooreweder, J. P. Kruth, J. Van Humbeeck, Changing the alloy composition of Al7075 for better processability by selective laser melting, *J. Mater. Process. Technol.* 238 (2016) 437–445.
- [57] P. Vora, R. Martinez, N. Hopkinson, I. Todd, K. Mumtaz, Customised Alloys Blends for In-situ Al339 alloy formation using anchorless selective laser melting, *Technologies* 5 (2017) 24.
- [58] J.M. Skelton, E.J. Sullivan, J.M. Fitz-Gerald, J.A. Floro, Efficacy of elemental mixing of in situ alloyed Al-33wt%Cu during laser powder bed fusion, *J. Mater. Process. Technol.* 299 (2022), 117379.
- [59] R. Della Gatta, I. Del Sol, A. Caraviello, A. Astarita, Selective laser melting of an Al-Si-Mg-Cu alloy: feasibility and processing aspects, *Mater. Manuf. Process.* 36 (2021) 1438–1449.
- [60] F. Bosio, D. Manfredi, M. Lombardi, Homogenization of an Al alloy processed by laser powder bed fusion in-situ alloying, *J. Alloy. Compd.* 904 (2022), 164079.
- [61] P. Wang, L. Deng, K.G. Prashanth, S. Pauly, J. Eckert, S. Scudino, Microstructure and mechanical properties of Al-Cu alloys fabricated by selective laser melting of powder mixtures, *J. Alloy. Compd.* 735 (2018) 2263–2266.
- [62] J.A. Glerum, S. Hocine, C.S.T. Chang, C. Kenel, S. Van Petegem, N. Casati, D. F. Sanchez, H. Van Swygenhoven, D.C. Dunand, Operando X-ray diffraction study of thermal and phase evolution during laser powder bed fusion of Al-Sc-Zr elemental powder blends, *Addit. Manuf.* 55 (2022), 102806.
- [63] A. Ivezović, N. Omidvari, B. Vrancken, K. Lietaert, L. Thijss, K. Vanmeensel, J. Vleugels, J.P. Kruth, Selective laser melting of tungsten and tungsten alloys, *Int. J. Refract. Met. Hard Mater.* 72 (2018) 27–32.
- [64] Q. Zhong, K. Wei, X. Yue, R. Zhou, X. Zeng, Powder densification behavior and microstructure formation mechanism of W-Ni alloy processed by selective laser melting, *J. Alloy. Compd.* 908 (2022), 164609.
- [65] C. Zhao, J. Yang, G. Li, Z. Wang, Laser powder bed fusion of the Mn-Cu alloys: printability, microstructure, and mechanical properties, *J. Alloy. Compd.* 899 (2022), 163385.
- [66] H. Li, S. Thomas, C. Hutchinson, Delivering microstructural complexity to additively manufactured metals through controlled mesoscale chemical heterogeneity, *Acta Mater.* 226 (2022), 117637.
- [67] K. Saeidi, L. Kevetkova, F. Lofaj, Z. Shen, Novel ferritic stainless steel formed by laser melting from duplex stainless steel powder with advanced mechanical properties and high ductility, *Mater. Sci. Eng. A* 665 (2016) 59–65.
- [68] K. Saeidi, L. Kevetkova, F. Lofaj, Z. Shen, Corrigendum to “Novel ferritic stainless steel formed by laser melting from duplex stainless steel powder with advanced mechanical properties and high ductility” [Mater. Sci. Eng. A 665 (2016) 59–65], *Mater. Sci. Eng. A*, 667, 2016, p. 250.
- [69] F. Hängsbach, P. Koppa, K. Duschik, M.J. Holzweissig, M. Burns, J. Nellesen, W. Tillmann, T. Tröster, K.P. Hoyer, M. Schaper, Duplex stainless steel fabricated by selective laser melting - microstructural and mechanical properties, *Mater. Des.* 133 (2017) 136–142.
- [70] S. Griffiths, M.D. Rossell, J. Croteau, N.Q. Vo, D.C. Dunand, C. Leinenbach, Effect of laser rescanning on the grain microstructure of a selective laser melted Al-Mg-Zr alloy, *Mater. Charact.* 143 (2018) 34–42.
- [71] B. Liu, B.Q. Li, Z. Li, Selective laser remelting of an additive layer manufacturing process on AlSi10Mg, *Results Phys.* 12 (2019) 982–988.